Novel Reconstruction and Feature Exploitation Techniques for Sensorless Freehand 3D Ultrasound

Hassan Rivaz[a], Hyun J. Kang[a], Philipp J. Stolka[a], Richard Zellars[b], Frank Wacker[c], Gregory Hager[a] and Emad Boctor[c]

Department of [a]Computer Science, [b]Radiation Oncology, and [c]Radiology, Johns Hopkins University

ABSTRACT

Out-of-plane motion in freehand 3D ultrasound can be estimated using the correlation of corresponding patches, leading to sensorless freehand 3D ultrasound systems. The correlation between two images is related to their distance by calibrating the ultrasound probe: the probe is moved with an accurate stage (or with a robot in this work) and images of a phantom are collected, such that the position of each image is known. Since parts of the calibration curve with higher derivative gives lower displacement estimation error, previous work limits displacement estimation to parts with maximum derivative. In this paper, we first propose a novel method for exploiting the entire calibration curve by using a maximum likelihood estimator (MLE). We then propose for the first time using constrains inside the image to enhance the accuracy of out-of-plane motion estimation. We specifically use continuity constraint of a needle to reduce the variance of the estimated out-of-plane motion. Simulation and real tissue experimental results are presented.

Keywords: 3D ultrasound, Speckle decorrelation, Fully developed speckle

1. INTRODUCTION

Most common techniques for acquiring 3D ultrasound data are oscillating head probes and freehand 3D ultrasound. In oscillating head probes, a 1D ultrasound transducer is automatically swept inside the probe, enabling 3D image acquisition. In freehand 3D ultrasound, a position sensor is attached to an ordinary probe which is swept over the desire region by the clinician.

Freehand 3D ultrasound is inexpensive, works with the existing 2D probes, and allows arbitrary 3D volume acquisition. However, the need for the additional sensor makes it difficult to use. Sensorless volume reconstruction of freehand 3D ultrasound is possible using the information in the images themselves: out of plane motion estimation can be obtained from image correlation,[1] which is the focus of this work, while in plane motion can be estimated through image registration[2–4] or by using techniques similar to elastography.[5–7]

The granular appearance of ultrasound images is the key factor in out-of-plane motion estimation (Figure 1). Each pixel in an ultrasound image is formed by the back-scattered echoes from an approximately ellipsoidal region called the resolution cell.[8] The interference of scatterers in a resolution cell creates the granular appearance of the ultrasound image, called speckle. Although of random appearance, speckle pattern is identical if the same object is scanned from the same direction and under the same focusing and frequency. Speckle characterization is essential in many areas of quantitative ultrasound. In this work, it is a prerequisite for speckle-based distance

Further author information: send correspondence to E-mail: rivaz@jhu.edu , eboctor1@jhmi.edu

estimation. We use low order moments to discriminate fully developed speckle (FDS) patches versus coherent speckle patches.[9]

$$R = \text{SNR} = \frac{\langle A^{v_r} \rangle}{\sqrt{\langle A^{2v_r} \rangle - \langle A^{v_r} \rangle^2}} \tag{1}$$

$$S = \text{skewness} = \frac{\left\langle (A^{v_s} - \langle A^{v_s} \rangle)^3 \right\rangle}{(\langle A^{2v_s} \rangle - \langle A^{v_s} \rangle^2)^{\frac{3}{2}}} \tag{2}$$

where A is the amplitude of the ultrasound RF envelope in the analysis patch, v_r and v_s are the signal powers and $\langle \cdots \rangle$ denotes the mean. Here we use[10] $v_r = 2v_s = 1$. An elliptical discrimination function is calculated in the R-S plane by performing principal component analysis (PCA) on the data from simulated FDS patches.[10] A patch is then classified as FDS if its R-S duple falls inside this ellipse.

Having found FDS patches in two ultrasound images, the correlation between them is used for estimating the distance between the two images.[11] The R-S metric requires approximately 3500 pixels per patch (depending on the correlation of data[12]), but such large patches (which are rectangles) of FDS are unlikely to be found in real tissue because of its inhomogeneity.[11] Gee et al.[13] proposed a heuristic technique that is robust to the lack of FDS patches in the ultrasound image. This method allows the calculation of the elevational distance for all patches of the image, regardless of their level of coherency, by measuring the axial and lateral correlation of each patch. Since the behavior of coherent reflectors in the elevational direction can be different from their behavior in the axial and lateral directions, the performance of the method can decline depending on the level of anisotropy of the tissue.

In,[14] we proposed a fast algorithm to find irregularly shaped FDS patches and showed that this algorithm finds significantly more FDS patches. Here, we use beam steering as another technique to increase the number of FDS patches found in the image.[15] This is achieved by obtaining more data from a certain region of tissue, hence reducing the size of the analysis patch. Having found such small FDS patches, we further use the steered images for better out-of-plane (elevational) motion estimation.

Coherent scattering causes the elevational distance measurement from the conventional correlation algorithms to be underestimated.[11] Thus, distance measurement is limited to the patches of the ultrasound image that contain only FDS.[11] To completely determine the out-of-plane degrees of freedom between two planes, at least three non-collinear pairs of such patches are required.[4]

Since FDS patches are extremely rare in real tissue, these methods usually have a low accuracy and are only relevant in limited tissue types. Gee et al.[13] proposed a heuristic technique that is robust to the lack of FDS patches in the ultrasound image. This method allows the calculation of the elevational distance for all patches of the image, regardless of their level of coherency, by measuring the axial and lateral correlation of each patch. Since the behavior of coherent reflectors in the elevational direction can be different from their behavior in the axial and lateral directions, the performance of the method can decline depending on the level of anisotropy of the tissue. The purpose of this work is to devise a method applicable to a various tissue types that accurately reconstructs 3D volumes from ultrasound images.

Recently, Laporte and Arbel[16,17] have proposed probabilistic fusion of noisy out-of-plane motion estimation. This work is most similar to these works, in that it calculates the maximum likelihood estimate (MLE) of the out-of-plane motion. We also use beam steering to obtain more data and increase the accuracy of the out of plane motion estimation similar to.[15]

2. METHODS

2.1. Combining Steered Images

We are looking for rectangular FDS patches using images acquired from the same location at different steering angles. The key idea is to combine data acquired from a certain region at different steering angles and therefore reducing the size of the analysis patch. Figure 2 shows two images acquired at 0 and θ steering angles. A

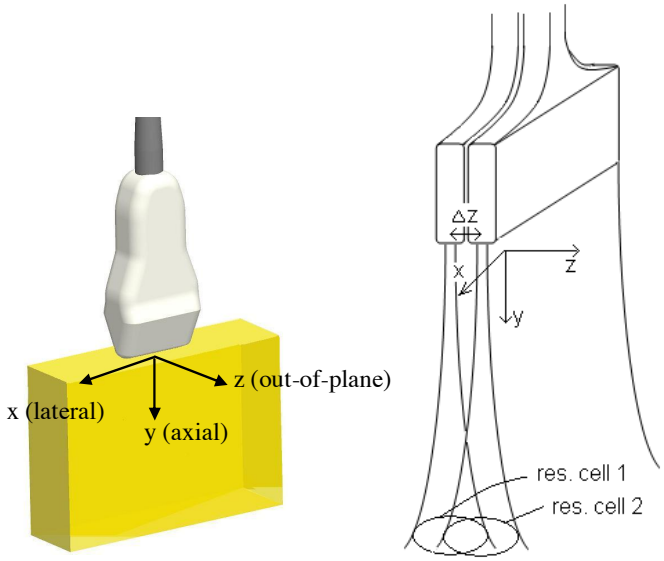

(a) Directions with respect to ultrasound probe

(b) Two ultrasound images overlapping the resolution cell

Figure 1. (a) shows the three directions relative to the ultrasound probe. Out-of-plane direction and elevational direction are used interchangably in this work. (b) shows aquisition of two ultrasound images at a distance of Δz. Ultrasound beam is in order of a millimeter wide. This wideness affects the resolution of ultrasound image in the lateral, y, and elevational, z, directions, as well as creating a granular pattern, called speckle. The size of the resolution cell in the axial direction, x, is determined by the wavelength of the ultrasound wave and is magnified in this image.

rectangle patch in the left image is warped into a parallelogram and is shifted in the steered right image. The position of the parallelogram can be simply found as a function of θ, x and y. Therefore, samples n_X and n_Y from the steered image correspond to samples n_x and n_y from the non-steered image and

$$\begin{aligned} n_X &= n_x - \frac{v_{US}}{2\nu} \cdot \frac{n}{w} \cdot \sin(\theta) \cdot n_y \\ n_Y &= \frac{n_y}{\cos(\theta)} \end{aligned} \tag{3}$$

where $v_{US} = 1540000$mm/s is the speed of ultrasound in tissue, ν is the sampling frequency of the ultrasound machine, n is the total number of the A-lines and w is the width of image in mm. To find the correspondence of a patch, the correspondent of its four corners are found using these equations and applying nearest neighbor interpolation. The parallelogram connecting these four corners is the correspondent of the patch.

2.2. Maximum Likelihood Motion Estimation

Assume we have two parallel ultrasound images with ground truth out-of-plane distance z (Figure 1), and that we have measured correlation coefficients ρ_i for $i = 1 \cdots n$ patches between the two images (Figure 3). The goal is to find μ_z which is maximum likelihood estimate of z given all the ρ_i measurements. Let $\rho_i = f_i(z_i)$ be the calibration function that relates the out-of-plane motion z_i to correlation coefficient ρ_i for patch i (each patch has a different calibration function depending on its depth, see Figure 6). Assuming that ρ_i is drawn from a Gaussian distribution with mean $f(\mu_z)$ and variance σ_i, the conditional probability of ρ_i is

$$\Pr(\rho_i \mid \mu_z, \sigma_i^2) = \frac{1}{(2\pi\sigma_i^2)^{1/2}} \quad e^{-\frac{(\rho_i - f_i(\mu_z))^2}{2\sigma_i^2}} \tag{4}$$

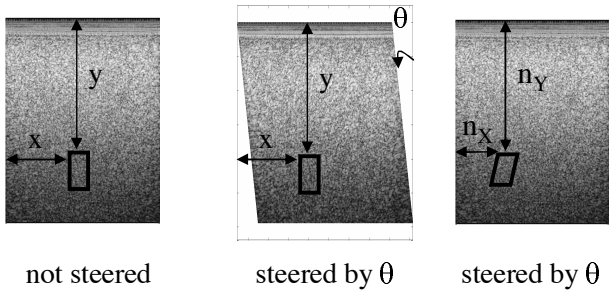

Figure 2. Corresponding patches in images acquired with different steering angles. In the left, a patch is shown in the not-steered image. In the middle, the patch which corresponds to the same tissue is shown in the scan-converted steered image. In the right, the patch is shown in the raw steered image (not scan-converted).

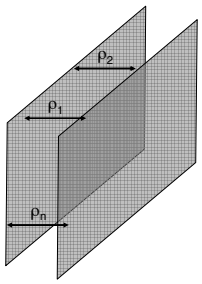

Figure 3. The correlation coefficient ρ_i is calculated between n patches of the two images.

We assume that ρ_i measurements are independent. Therefore, the conditional probability of observing all the ρ_i values will be simply their multiplication. Looking at the product as a function of μ and σ_i and taking its logarithm to convert multiplication to summation, we have the familiar log-likelihood equation

$$L(\vec{\rho}|\ \mu_z, \vec{\sigma^2}) = -\Sigma_{i=1}^{n}\left[\frac{1}{2}\log\sigma_i^2 + \frac{(\rho_i - f_i(\mu_z))^2}{\sigma_i^2}\right] + \frac{n}{2}\log(2\pi) \tag{5}$$

where $\vec{\rho}$ and $\vec{\sigma^2}$ are two vectors containing all the ρ_i and σ_i^2 measurements. In the above equation, ρ_i is the correlation of two corresponding patches and is known. σ_i^2 is also known: it is the variance of the correlation and is calculated in the calibration process (Figure 6). To find the ML estimate of the μ_z, we differentiate this equation with respect to μ_z and set it to zero, arriving at

$$\Sigma_{i=1}^{n}\frac{f_i'(\mu_z)(\rho_i - f_i(\mu_z))}{\sigma_i^2} = 0 \tag{6}$$

where f' denotes derivative of f. Unfortunately this equation is not easy to solve for μ_z. Instead, lets transform ρ_i to z_i and write the log-likelihood functions in terms of z_i's. Equation 5 becomes

$$L(\vec{z}|\ \mu_z, \vec{\sigma_z^2}) = -\Sigma_{i=1}^{n}\left[\frac{1}{2}\log\sigma_{zi}^2 + \frac{(z_i - \mu_z)^2}{\sigma_{zi}^2}\right] + \frac{n}{2}\log(2\pi) \tag{7}$$

where $\sigma_{zi}^2 = \frac{\sigma_i^2}{f'(\rho_i)^2}$ is the transformed variance in the ρ domain (σ_i) to the z domain (σ_{zi}). Differentiating with respect to μ_z and setting it to zero gives

$$\Sigma_{i=1}^{n}\frac{z_i - \mu_z}{\sigma_{zi}^2} = 0 \tag{8}$$

which can be easily solved to give

$$\mu_z = \frac{\Sigma_{i=1}^{n} \frac{z_i}{\sigma_{zi}^2}}{\Sigma_{i=1}^{n} \frac{1}{\sigma_{zi}^2}} \tag{9}$$

Finally, we utilize constraints in the images to enhance out-of-plane motion estimation. Many surgical procedures such as biopsy, drug delivery and brachytherapy involve inserting a needle into the tissue. The prior of needle continuity can be used to decrease the variance of the measured out of plane motion (we are assuming that the needle crosses US image plane and is not parallel to the image). Assume that the tip of the needle can be measured at each image with a variance of $[\sigma^*_{needle}]^2$, and that the angle of the needle with the normal of the ultrasound image (i.e the angle between the needle and the axes y in Figure 1) is α. Also, let $\sigma^2_{cor.}$ denote the variance of the out-of-plane motion estimation using the correlation method and $\sigma_{needle} = \sigma^*_{needle} / \tan(\alpha)$. Assuming both noises are Gaussian, variance of the final estimate which combines the two estimates is $\frac{\sigma^2_{needle}\sigma^2_{cor.}}{\sigma^2_{needle}+\sigma^2_{cor.}}$. It can be easily shown that this quantity is less than both σ^2_{needle} and $\sigma^2_{cor.}$, meaning that the resulting variance is less than both initial variances.

2.3. Calibration and Data Acquisition

The system operates in two distinct modes - calibration mode and image-based 3DUS reconstruction mode (Figure 4). Both will be described from a process flow perspective. In the calibration mode, information necessary to calibrate the distance estimations is collected (Figure 4). To this end, the robot control component steps the robot through a series of precisely defined positions and triggers the acquisition of a single US frame (RF data) at each position from a homogeneous fully developed speckle (FDS) phantom. These frames are associated with their respective coordinates and stored for offline use. Then, the software system reads the batch of frames and positions and subdivides the frames into distinct subpatches. Pairs of patches from the same location originating from frames at different distances are correlated, thus creating a set of (strictly monotonous) calibration (or decorrelation) curves x,y(d). These curves depend on the characteristics of the selected probe, the imaging frequency, and the image location x, y (in particular the depth y) of the respective patches. Currently, the offline calibration process takes 2-3 minutes including scan time to generate the needed calibration curves (decorrelation curves). Before this recent development, manual data collection and offline processing using MATLAB scripts used to take many hours of effort.

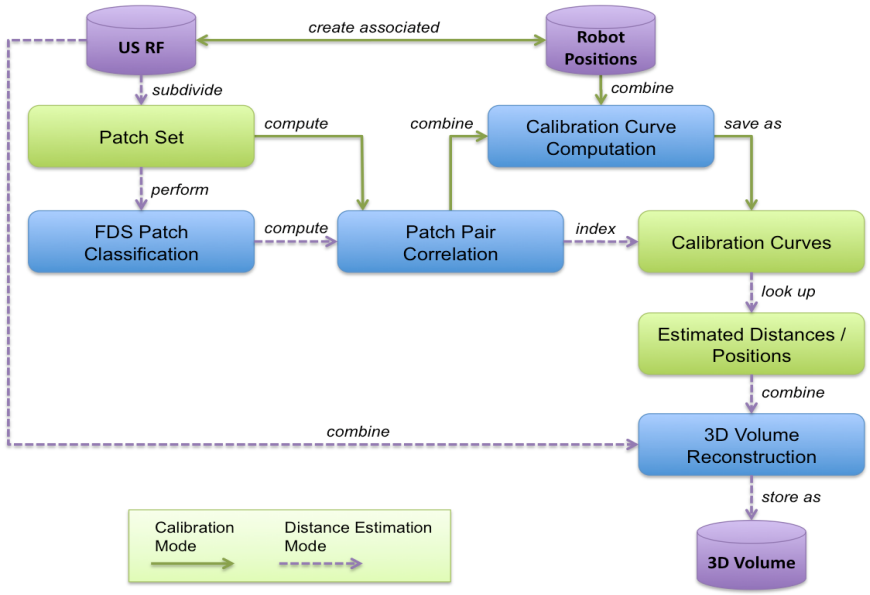

Figure 4. The data acquisition and calibration system (some of the blocks are the subject of future work).

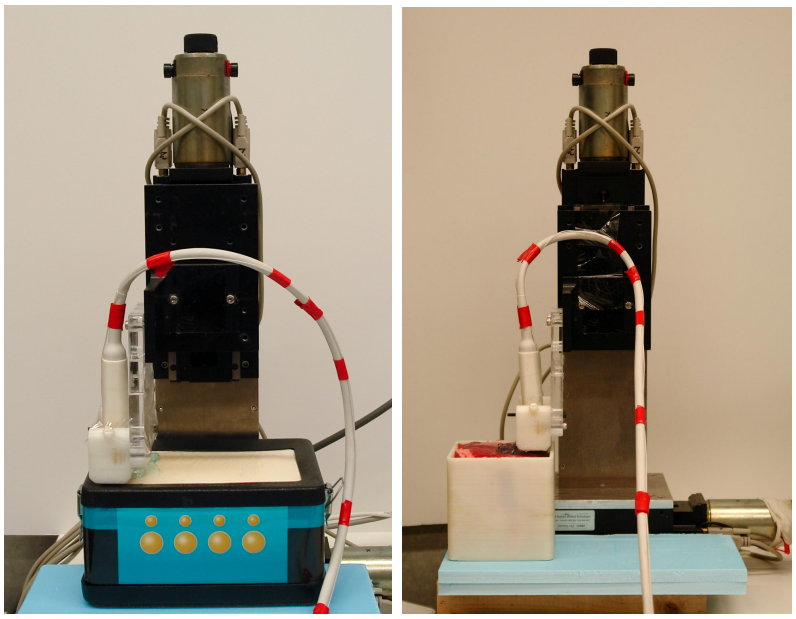

(a) Calibration experiment

(b) Out-of-plane motion estimation using real tissue

Figure 5. The experimental setup for moving the probe out-of-plane and acquiring ultrasound images. In (a), the robot moves the probe in the out-of-plane direction while the ultrasound is imaging a FDS phantom to generate the calibration curves. In (b), the robot is moving the probe while the ultrasound is imaging real tissue, so that the speckle correlation results can be compared to ground truth (i.e. robot readings).

3. EXPERIMENTAL SETUP

The ultrasound RF data was sampled with a robot-based system in order to achieve reliable, high-accuracy ground truth readings for the displacements. This will give us the images we need for calibration and also the gives us the ground truth when we reconstruct the volume. This process yielded a series of planar-parallel RF slices through the respective phantom, in a fashion somewhat comparable to a freehand sweep. The phantoms were positioned within the workspace of a high-precision three degrees-of-freedom (DoF) cartesian robot stage (DMC-21x3 with three servo motor stages, by Galil Motion Control; relative accuracy better 0.005 mm). For calibration, the stage translated the probe to new positions every $\Delta x = 0.05\ mm$ apart, then triggered RF slice acquisition via a TTL signal connected to the ultrasound machine's ECG trigger port, where the data was written to file. For calibration data acquisition, a FDS phantom is imaged. For volume reconstruction, real tissue (beef steak) is used. Figure 5 shows the experimental setup.

An Ultrasonix ultrasound machine (Burnaby, BC) with a sampling frequency of $\nu = 20$MHz is used to acquire RF data. To calibrate the rate of image decorrelation with out-of-plane motion, RF data of 5x80 parallel frames were acquired from a FDS phantom at an elevational distance of 0.05 mm between consecutive images: five frames at each location with steering angles of -5, -2.5, 0, 2.5 and 5.5 degrees. The experimental setup is shown in Figure 5: the probe is moved with a micrometer with the accuracy of .005 mm. Calibration results showed that the decorrelation rate is not affected by beam steering.

Out-of-plane motion estimation was performed on ex-vivo beef steak tissue. 4x80 RF frames at an elevational distance of 0.05 mm between consecutive frames were acquired using the setup shown in Figure 5: four images at each location with $-5°$, $-2.5°$, $0°$, $2.5°$ and $5°$ steering angles.

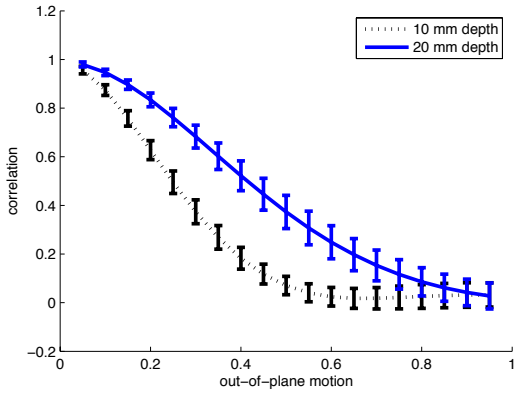

Figure 6. Two calibration curves at depths of 10 mm and 20 mm and their variances. Note that the calibration curve at the deeper location drop slower with the out-of-plane motion.

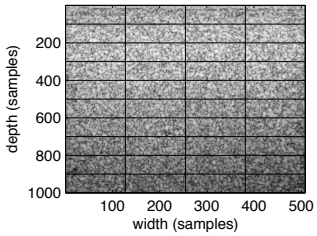

Figure 7. Subdivision of an image of the FDS phantom into patches is shown.

4. OUT-OF-PLANE MOTION ESTIMATION

The correlations are calculated using Pearsons linear correlation coefficient ρ

$$\rho(W,Z) = \frac{\Sigma w_i z_i - N\mu_w\mu_z}{\sqrt{\left(\Sigma w_i^2 - N\mu_w^2\right)\left(\Sigma z_i^2 - N\mu_z^2\right)}} \tag{10}$$

where w_i and z_i, $i = 1 \cdots N$, are the intensity values of each pixel in patches W and Z, N is the total number of pixels and μ_w and μ_y are the means of the intensity values of patches W and Z respectively.

Patches that are closest to being FDS are selected as described in.[15] Figure 8 shows the results of reconstructing out-of-plane motion using the correlation values. (a) and (b) are obtained by combining the two images with $\pm 2.5°$ steering angle at each location, while (c) and (d) are obtained by combining the two images with $\pm 5°$ steering angle at each location. The results show that using the MLE method slightly reduces both the underestimation error and the variance of the out-of-plane measurements. IN addition, it can be seen from (b) and (d) that the needle constraint reduces the variance in the measurements.

5. DISCUSSION AND CONCLUSION

Out-of-plane motion estimation is only studied here for a fixed distance between two frames, 0.4mm. A study of accuracy as the distance varies gives insight for optimum frame selection.[18,19] In freehand experiments the images are not parallel as they are in our experiments, and therefore the rotations between the images need to be found.[11,13,20] We showed before[15] that performing beam steering significantly increases the accuracy of out-of-plane motion estimation. In this work, we showed that MLE can also be used to enhance the out-of-plane motion estimation.

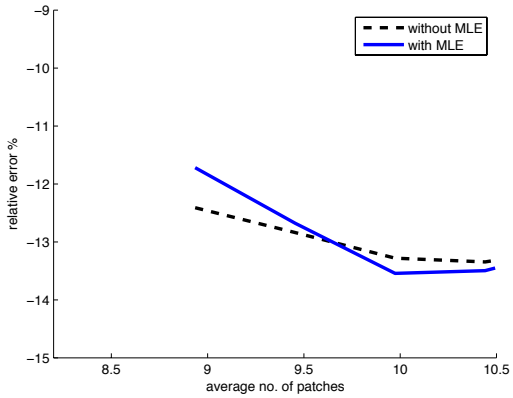

(a) relative error, $\pm 2.5^\circ$ steering angle

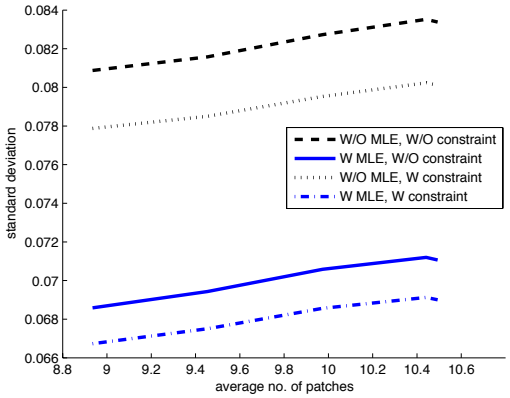

(b) standard deviation, $\pm 2.5^\circ$ steering angle

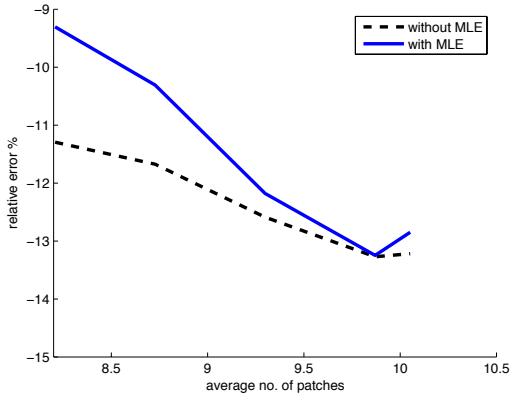

(c) relative error, $\pm 5^\circ$ steering angle

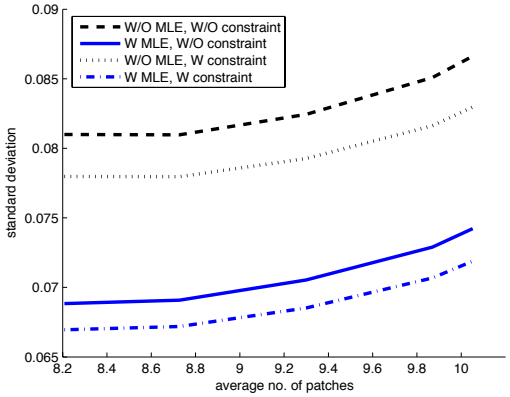

(d) standard deviation, $\pm 5^\circ$ steering angle

Figure 8. relative error and standard deviation of the sensorless measurements. (a) The relative error. Reconstruction is performed using two steered images at $\pm 2.5^\circ$. (b) The standard deviation of the measurements. W/O MLE refers to without MLE, W/O constraint refers to without utilizing the needle continuity constraint, and W MLE refers to with MLE. (c) and (d) are corresponding errors and variances with two steered images at $\pm 5^\circ$.

Acknowledgment

H. Rivaz is supported by the DoD Predoctoral Traineeship Award and by the Advanced Simulation Fellowship from the Link Foundation.

REFERENCES

1. J. Chen, B. Fowlkes, P. Carson, and J. Rubin, "Determination of scan-plane motion using speckle decorrelation: theoretical considerations and initial test," *Imag. Sys. and Tech.* **8**, pp. 38–44, 1997.
2. G. Treece, R. Prager, A. Gee, C. Cash, and L. Berman, "Correction of probe pressure artifacts in freehand 3D ultrasound," *Medical Image Analysis* **6**, pp. 199–215, 2002.
3. B. Geiman, L. Bohs, M. Anderson, S. Breit, and G. Trahey, "A novel interpolation strategy for estimating subsample speckle motion," *Pattern Recog. Letters* **45**, pp. 1541–1552, 2000.
4. R. Prager, A. Gee, G. Treece, C. Cash, and L. Berman, "Sensorless freehand 3-d ultrasound using regression of the echo intensity," *Ultrasound Med. Biol.* **29**, pp. 437–446, 2003.
5. H. Rivaz, E. Boctor, P. Foroughi, G. Fichtinger, and G. Hager, "Ultrasound elastography: a dynamic programming approach," *IEEE Trans Med Imaging* **27**, pp. 1373–1377, Oct. 2008.
6. H. Rivaz, I. Fleming, L. Assumpcao, G. Fichtinger, U. Hamper, M. Choti, G. Hager, and E. Boctor, "Ablation monitoring with elastography: 2d in-vivo and 3d ex-vivo studies," *Medical Image Computing & Computer Assisted Interventions, MICCAI, New York, NY* , pp. 458–466, Sept. 2008.
7. H. Rivaz, P. Foroughi, I. Fleming, R. Zellars, E. Boctor, and G. Hager, "Tracked regularized ultrasound elastography for targeting breast radiotherapy," *Medical Image Computing & Computer Assisted Interventions, MICCAI, London, UK* , pp. 507–515, Sept. 2009.
8. R. Wagner, S. Smith, J. Sandrik, and H. Lopez, "Statistics of Speckle in Ultrasound B-Scans," *IEEE Trans. Sonics and Ultrasonics* **17**(3), pp. 251–268, 1983.
9. R. Prager, A. Gee, G. Treece, and L. Berman, "Analysis of speckle in ultrasound images using fractional order statistics and the homodyned k-distribution," *Ultrasonics* **40**, pp. 133–137, 2002.
10. H. Rivaz, E. Boctor, and G. Fichtinger, "Ultrasound speckle detection using low order moments," *IEEE Int. Ultrasonics Symp.* , pp. 2092–2095, Oct. 2006.
11. P. Hassenpflug, R. Prager, G. Treece, and A. Gee, "Speckle classification for sensorless freehand 3-d ultrasound," *Ultrasound Med. Biol.* **31**, pp. 1499–1508, Nov. 2005.
12. V. Dutt and J. Greanleaf, "Speckle analysis using signal to noise ratios based on fractional order moments," *Ultrasonic Imag.* **17**, pp. 251–268, 1995.
13. A. Gee, R. Houdson, P. Hassenpflug, G. Treece, and R. Prager, "Sensorless freehand 3d ultrasound in real tissue: Speckle decorrelation without fully developed speckle," *Medical Image Analysis* **10**, p. 137:149, Apr. 2006.
14. H. Rivaz, E. Boctor, and G. Fichtinger, "A robust meshing and calibration approach for sensorless freehand 3d ultrasound," *Proc. SPIE Medical Imaging* **6583**, pp. 181–188, Feb. 2007.
15. H. Rivaz, R. Zellars, G. Hager, G. Fichtinger, and E. Boctor, "Beam steering approach for speckle characterization and out-of-plane motion estimation in real tissue," *IEEE Int. Ultrasonics Symp.* , pp. 781–784, Oct. 2007.
16. C. Laporte and T. Arbel, "Combinatorial and probabilistic fusion of noisy correlation measurements for untracked freehand 3-d ultrasound," *IEEE Trans Med Imaging* **27**, pp. 984–994, Jul. 2008.
17. C. Laporte, J. Clark, and T. Arbel, "Generalized poisson 3-d scatterer distributions," *IEEE Trans. Ultrason. Ferroelectr. Freq. Control* **56**, pp. 410–414, Feb. 2009.
18. W. Smith and A. Fenster, "Optimum scan spacing for three-dimensional ultrasound by speckle statistics," *Ultrasound Med. Biol.* **26**, pp. 551–562, May 2000.
19. W. Smith and A. Fenster, "Analysis of an image-based transducer tracking system for 3d ultrasound," *Proceedings of SPIE - The International Society for Optical Engineering* **5035**, pp. 154–165, 2003.
20. J. Housden, A. Gee, R. Prager, and G. Treece, "Rotational motion in sensorless freehand 3D ultrasound," *Univ. of Cambridge Tech. Rep.* , Oct. 2007.